Available online at www.sciencedirect.com
SCIENCE DIRECT®
International Journal of Heat and Mass Transfer 48 (2005) 1236–1251
International Journal of HEAT and MASS TRANSFER
www.elsevier.com/locate/ijhmt

Convective heat transfer from a partially premixed impinging flame jet. Part I: Time-averaged results

S.G. Tuttle [a,1], B.W. Webb [a,*], M.Q. McQuay [a,2]

[a] Department of Mechanical Engineering, Brigham Young University, Provo, UT 84602, United States

Received 5 April 2004; received in revised form 11 October 2004
Available online 15 December 2004

Abstract

Axial and radial profiles of time-averaged local heat fluxes of methane–air jet flames impinging normal to a cooled plate are reported, as functions of equivalence ratio, Reynolds number, and nozzle-plate spacing. Time-resolved behavior for these conditions is examined in the companion paper, Part II. Flame structure was studied visually and photographed. Both premixed and diffusion flame behavior was observed. Nozzle-stabilized flames revealed a stable, axisymmetric flame structure at nozzle-plate spacings less than 14 diameters. At greater nozzle-plate spacings, buoyancy-induced instabilities caused the flame to oscillate visibly. Lifted flames exhibited varied flame structures dependent upon the Reynolds number, equivalence ratio, and nozzle-plate spacing, stabilizing in the free jet, at the stagnation zone, or downstream in the wall jet. Local heat flux measurements made in the stagnation zone and along the plate adjacent to the wall jet flame revealed correlation of the local heat flux to the flame structure. Negative heat fluxes resulted from cool gases impinging on the hotter plate. The magnitude of positive heat fluxes depended on the proximity of the flame to the sensor surface, the rate of heat release, and the local molecular and turbulent transport.

1. Introduction

Flame impingement heat transfer has been studied extensively due to its practical application in the heating or drying of material in industrial and domestic processes. This method is being increasingly used in heating processes rather than more expensive radiant heating techniques. The greater heat fluxes obtained with flame impingement have been found to reduce the processing time and costs while increasing product quality [1]. It also has the advantage of being a quick, localized method that allows more precise heating control over a specific area than radiant heating methods.

Only recently have variations in local wall heat flux from impinging flame jets begun to be explored and understood, although there is substantial information collected for various flow conditions and fuels. This is perhaps due to the instrumentation used to date having measured the heat flux over large areas and/or large thermal capacitance due to the mass of the sensor [2]. Developments in thermopile construction have produced small sensors that can be used to make localized measurements of heat flux. The localized time-averaged measurements that have been made possible with this instrumentation have provided insight into how the

* Corresponding author. Tel.: +1 801 422 6543; fax: +1 801 422 0516.
E-mail address: webb@byu.edu (B.W. Webb).
[1] Present address: Pratt & Whitney, Hartford, CT.
[2] Present address: Oblon, Spivak, McClelland, Maier & Neustadt P.C., 1940 Duke Street, Alexandria, VA 22314.

0017-9310/$ - see front matter © 2004 Elsevier Ltd. All rights reserved.
doi:10.1016/j.ijheatmasstransfer.2004.10.027

Nomenclature

d	nozzle diameter
h	nozzle-plate spacing
H	dimensionless nozzle-plate spacing, h/d
q''	local time-mean heat flux
r	radial distance from stagnation point
R	dimensionless radial distance from stagnation point, r/d
Re	nozzle Reynolds number, based on nozzle diameter and physical properties of the unburned methane–air mixture at the nozzle exit, $\rho V d/\mu$
V	Average fluid velocity at nozzle exit
f_s	Sampling frequency
Greek symbols	
Φ	equivalence ratio, the ratio of the stoichiometric to actual air-to-fuel ratio, $\Phi = (A/F)_{stoich}/(A/F)_{act}$
μ	gas mixture dynamic viscosity
ρ	gas mixture density

local heat flux behavior reflects the flame structure at the plate surface.

There has already been a great deal of research done in this area. Early work by Hargrave et al. was among the first to explore the physics of flame structure and corresponding heat transfer for impinging flame jets [5,6]. Relatively recent reviews by Viskanta [1,3,4] and Baukal and Gebhart [2,7–9] summarize the results of studies prior to their publication date, and call attention to areas that have yet to be explored. Since these comprehensive reviews, there has been additional work addressing the fundamentals of flame jet impingement heat transfer under a variety of configurations. Some studies have focused more on the combustion characteristics of impinging flames [10–14]. However, a considerable body of recent literature has focused on heat transfer behavior of impinging jet flames. A number of careful investigations have explored heat transfer under single circular or slot jet flames [15–19]. Additionally, several recent studies have characterized the heat transfer in a multiple-jet configuration [20–25].

Despite a growing body of literature related to flame jet impingement heat transfer, the unsteady characteristics of the impingement heat transfer have gone unexplored. These two papers, Parts I and II, seek to document the local heat flux behavior for an impinging, partially premixed circular methane jet over a broad range of Reynolds number, equivalence ratio, nozzle-plate spacing, and radial location along the impingement plate. Part I focuses on observed flow structure for the experimental conditions studied and corresponding local measured time-mean heat transfer along the impingement plate, while time-resolved measurements are reported and discussed in Part II. While the heat transfer phenomena are linked in a complex way to the combustion process, the focus here is on local wall flux characteristics. However, the heat transfer is correlated to observed flame structure, which is documented photographically. It is hoped that this work will not only serve as a reference for design engineers, but also provide insight into the unsteady flame impingement heat transfer for various flow conditions. Further, the information reported here provides benchmark data against which modeling results may be compared.

2. Experimental method

Fig. 1 illustrates schematically the experimental apparatus used for visually observing the flame structure, and measuring the instantaneous local flame impingement heat flux. The details of the cooled impingement plate, heat flux sensors, flame jet, and flow control of the methane and air are described below.

The impingement plate, measuring 71 cm square, was fabricated of two layers of aluminum plate separated by a rubber seal. The bottom plate, exposed to the impinging flame, was 1.27 cm thick 7075-T6 aluminum with milled parallel grooves through which cooling water flows. This square plate was divided into three rectangular zones, through each of which a separate cooling channel was milled. A hole was drilled and tapped in the center for mounting the heat flux sensor. The top plate was 0.635 cm thick 6065-T5 with holes for attaching it to the structure over the burn chamber and accessing the sensor. The flow of the cooling water was regulated with three calibrated variable area flow meters. Thermocouples measured the temperature of the water flowing in and out of the plate to maintain the plate at a near-constant temperature. Heated water, at temperatures in the range 40–50 °C, was used as the plate coolant to prevent moisture in the combustion products from condensing on the impingement plate. The approximate 10 °C variation in plate temperature was assumed negligible in comparison to the impinging flame temperature at the plate. The surface of the impingement plate was polished smooth in its fabrication, and was uncoated. The experimental conditions selected for study

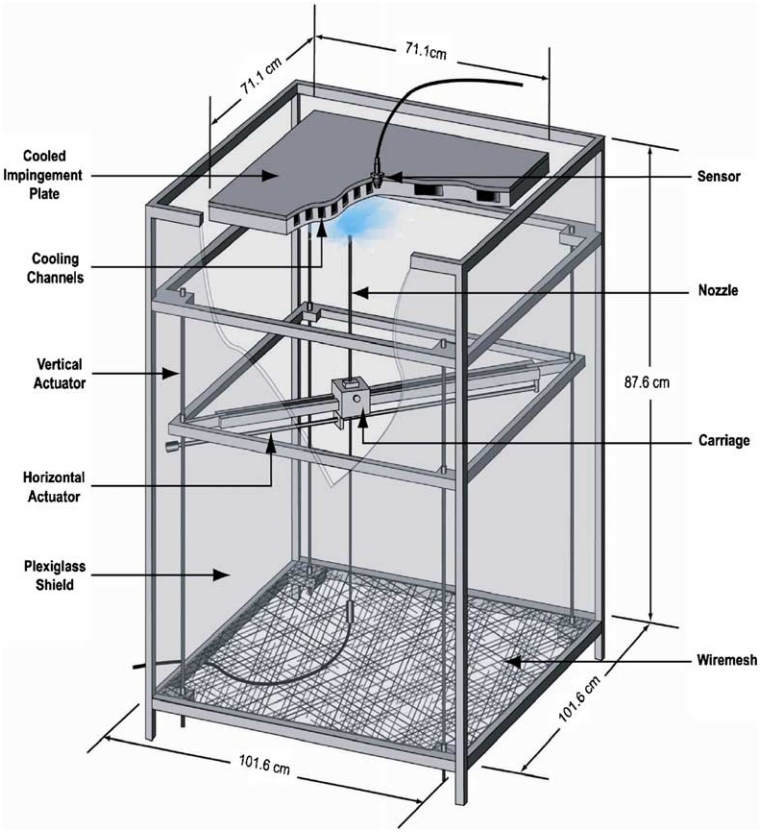

Fig. 1. Experimental apparatus used in the study.

avoided soot formation, so there were no soot deposits on the surface. Thus, the flame impinged against polished aluminum during all tests. Nevertheless, as a precaution the surface was periodically cleaned.

A Vatell HFM-7-E/L heat flux sensor was placed at the center of the impingement plate to measure the local heat flux and plate temperature. It was comprised of a differential thermopile to measure heat flux and a resistive temperature sensor embedded in aluminum nitride surrounded by a copper casing. The uncoated (low-emissivity), active region of the heat flux gage is a circle approximately 3 mm in diameter. The thermopiles were of composition 90% Nickel–10% Chromium/Constantan, and the resistive temperature sensor was platinum. The thermopile, embedded in the face of the sensor, produced a voltage that varied with the temperature gradient in the aluminum nitride at the face of the sensor [26]. According to the manufacturer's specifications, these uncoated sensors have a response time of 2–6 μs. The sensor was inserted in the water-cooled aluminum impingement plate such that the face of the sensor was exactly flush with the impingement surface. Due to their small size and copper casing, it may be safely assumed that the sensor does not introduce a thermal discontinuity in the plate. The sensor was connected to a Vatell AMP-6 amplifier by shielded, grounded wire to reduce ambient noise. The amplified voltages were connected to a Sheldon Instruments DB1 I/O card, linked to a coupled SI-DSP6400-R1 daughter card and a SI-C31DSP PCI card for 16-bit A/D conversion in a Hewlett-Packard Vectra VL personal computer. Local, time-average heat fluxes were calculated by averaging 2^{18} data points in each location where measurements were made. The calculation details of the time-resolved measurements are presented in the companion paper (Part II).

The nozzle was a stainless steel tube with an inner diameter $d = 6.6$ mm, wall thickness 0.8 mm, and length $l = 600$ mm ($l/d = 91$). It was attached to a carriage that permitted travel across a track, controlled by the horizontal positioner, to change the radial position of the flame jet with respect to the fixed sensor location. The carriage was also translated vertically by vertical positioners (four threaded rods) to change its height with respect to the plate. The vertical and horizontal movement served not only to translate the flame with respect to the sensor, but also as an aid in registering the distance from the stagnation point to prominent structures observed visually in the flame. The flame chamber was 88 cm high

and 102 cm square and enclosed on all four sides by 4.8 mm-thick Plexiglass. Below the carriage were two layers of wire mesh screens to minimize the influence of air currents present in the laboratory on the flow behavior of the flame.

Flames were photographed using a 35 mm SLR Kodak Max 400, with the aperture set at 5.6 and the *f*-stop set between 15 and 20, depending on the size and brightness of the flame. While photographing the flames, two of the Plexiglass panels were removed from the combustion enclosure to eliminate multiple reflections. Care was taken during the photographic documentation that removal of the panels caused no disturbance to the flame structure.

The air and methane flow rates were controlled with variable-area flow meters, calibrated for laboratory ambient pressure and temperature. Thermocouples were placed in fittings upstream of the flow meters to measure the temperature of the methane and air. The calibration accuracy for the flow meters was 5.8%. Both the air and methane were fed into a mixing chamber/flame arrestor, traveling through a tube to the nozzle in the burn chamber. The flame arrestor was a 16 cm-long, 4 cm-diameter cylinder filled with 4.5 mm steel ball bearings to serve as a mixing chamber and to quench any possible flame flashback from the nozzle exit.

3. Experimental uncertainty

The uncertainty for the Reynolds number, equivalence ratio, and heat flux were determined using methods described by Moffat [27]. The uncertainties for the Reynolds number and equivalence ratio were both determined to be in the range of 6%. For the mean heat flux measurements, the uncertainty due to the instrumentation was ± 3.4 kW/m^2 [28].

4. Experimental conditions

Local, time-resolved heat flux measurements and photographs were collected for Reynolds numbers in the range 1500–6000, based on nozzle exit conditions. For this study of flame impingement normal to a flat plate there are two dimensionless parameters used, $H = h/d$, and $R = r/d$, to specify nozzle-plate spacing and radial location, respectively [7]. Radial heat flux profiles were gathered only at locations along the plate from the stagnation point to the visible tip of the flame. Flame symmetry about the nozzle axis was verified visually, and by limited heat flux measurements along a radial line on both sides of the stagnation point [28]. Equivalence ratios were limited to eliminate the formation of soot in any of the flames which would result in deposits on the sensor surface. For flames at nozzle Reynolds numbers of 1500, the equivalence ratio was varied between unity (premixed) and seven (diffusion). For a Reynolds number of 2800, the equivalence ratio was varied from 3.7 to 8.9. For flames at a nozzle Reynolds number of 5600, the equivalence ratio was varied between 3.7 and 7.4. Given the non-sooting (non-luminous) flame conditions studied, the net radiation flux to the plate was estimated to be no greater than 1.8 kW/m^2, which is less than the experimental error in mean flux. Consequently, no correction to the measurements has been made, and the data reported herein may be viewed as convective flux.

5. Results and discussion

The time-averaged heat flux data will be presented and discussed in this section. Due to the dependence of the heat flux on flame structure and stabilization regime, the observed flame behavior will be discussed first to facilitate the understanding of the heat flux results presented later. Only a subset of the heat flux data collected in this investigation is presented here to illustrate the phenomena due to space limitations. For all of the results, the reader is referred to Tuttle [28].

The results will be presented in the following sequence: A base-case flame structure will be described and analyzed. This will be followed by comparisons of structure and behavior changes that occurred when the normalized nozzle-plate spacing (H), equivalence ratio (Φ), or nozzle Reynolds number (Re) were independently varied; as one parameter was changed, the others were maintained constant to observe the effect of the varied parameter on the flame structure and the local time-averaged heat flux. The discussion of the local heat flux will follow, with the same organization as the flame behavior discussion.

5.1. Flame behavior

The combustion regime (premixed or diffusion-controlled) and the location of the flame stabilization point characterized the different flame behavior observed in this investigation. Premixed combustion stabilizes where the local flow velocity is equal to the local laminar flame velocity, which is controlled mainly by thermal diffusivity and reaction rate. In a laminar flow, a fuel-rich premixed flame will have inner and outer cones of combustion; the inner cone is the location at which combustion will initially stabilize forming a bright blue flame. Secondary, diffusion-controlled combustion occurs at the outer cone. It is also known that in turbulent flows the location where the flame stabilizes will fluctuate as turbulence in the flow changes the local velocities over time. Consequently, the flame may appear, to the eye, thicker or more voluminous than it actually is as

it moves and/or spreads within a region where the local flow velocity is equal to the laminar flame speed [29]. Diffusion flames, in addition to being affected by the local velocity flow field, are controlled by the molecular or turbulent transport of the fuel and oxidizer. The flame stabilizes where the local fuel and oxidizer concentrations are stoichiometric. This results in a thin, luminescent flame surface at the interface between the fuel and oxidizer [29,30].

The nomenclature of the flow field structures and regions, used to describe the location of the flame stabilization point and the flame structure, are shown in Fig. 2a and b (adapted from [1]). Generally, the structure of the impinging jet of a mixture of fuel and air, in Fig. 2a, has three principle regions: the free jet, the stagnation zone, and the wall jet. In the free jet, the shear layer between the exiting jet and the ambient air drives the transport of momentum, energy, and mass. With an increase in the axial distance from the nozzle exit, the diameter of the free jet increases, the temperature of the jet changes, the entrained ambient air increases the overall mass flow rate impinging the plate, and the average velocity decreases. If there is a sufficient decrease in the local velocity and either (i) the local equivalence ratio reaches a stoichiometry for a diffusion flame, or (ii) the overall stoichiometry is within flammability limits for a premixed flame, due to the shear layer between the jet and the surrounding air, the flame will stabilize in the free jet. In the stagnation zone, the flow impinges on the plate and begins to flow radially along the plate. Here, there is little entrainment in comparison to what occurs in the free jet, but the change in direction can decrease the velocity enough to allow the flame to stabilize in that region. The wall jet region is characterized by radial flow along the face of the impingement plate that decreases in velocity with distance from the stagnation point [4]. If the flame has not stabilized in the free jet and the stagnation zone, the flame will stabilize in the wall jet if the entrained air has not decreased the fuel concentration below the flammability limit.

The pre-impingement jet itself, in Fig. 2b, also has three characteristic regions: a potential core, a developing region, and a fully developed region. A central region, where the gases have the same temperature, species concentration, and velocity as those found at the nozzle exit, characterizes the potential core. Unless the initial fuel and oxidizer proportions are within flammability limits and flow rate conditions are within flashback and blow-off limits, the flame will not stabilize in the core. It is in the regions surrounding the core, where mass, momentum, and energy transport to and from the surrounding air penetrates the core, reducing the local velocities and changing the local concentrations sufficiently to allow the flame to stabilize. In the developing region, the shear stress between the jet and the ambient air causes the axial velocity to continue to decay. The large shear stresses in that region also drive the generation of turbulence and create regions where the jet entrains and mixes with the ambient air, again creating another region where the local velocities and concentrations may allow combustion to stabilize. Beyond the developing region, velocity and concentration profiles are fully developed, the local jet diameter continues to increase and the local average velocity at a given radial location decreases with increasing axial distance from the jet exit. This provides, with sufficient distance, a flame stabilization point, if the local methane concentration has not decreased below the flammability limit. All three of the regions of the free jet are characterized by an increasing jet diameter with axial distance from the nozzle as the jet entrains ambient air [4].

A qualitative map of the different flame structures visually observed in this investigation is shown in Fig. 3 as a function of equivalence ratio and Reynolds num-

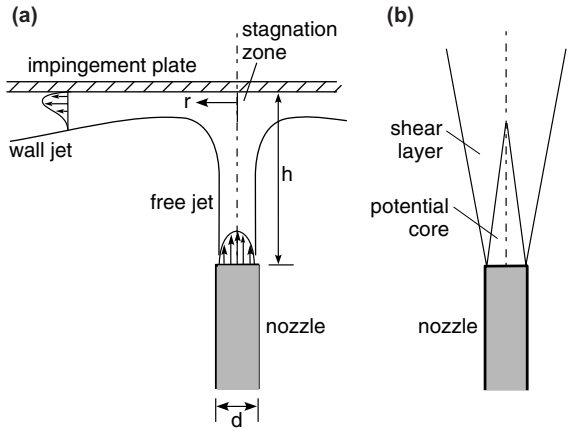

Fig. 2. Schematic diagram of an impinging jet flow illustrating the structure and traditional nomenclature of (a) an impinging jet and (b) a free jet (adapted from [4]).

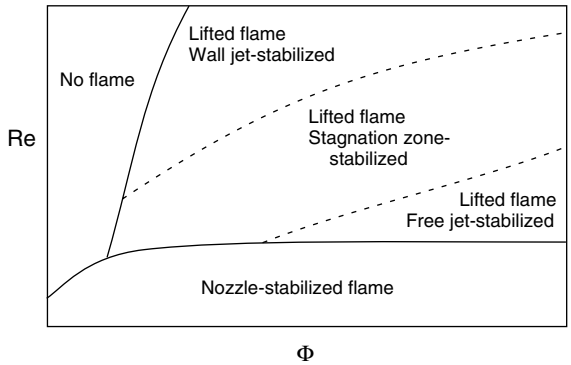

Fig. 3. Flame structure map as a function of equivalence ratio and Reynolds number.

ber for all of the nozzle-plate spacings studied. The flames discussed herein are either nozzle-stabilized or lifted flames, as customarily described in the literature [29–32]. Lifted flames were further observed to stabilize in the free (pre-impingement) jet, stagnation zone, or wall jet. Fig. 3 will serve as a reference in understanding the mechanism for transitions that will be described in the discussion of the flame structure. The dashed line delineating the different lifted flame structures denote gradual transitions from one regime to the other. Because this investigation is concerned principally with heat transfer, the physics of flame stabilization mechanisms are outside its scope and will not be discussed. The reader is referred elsewhere for recent investigations into the stabilization mechanisms of laminar and turbulent flames [33–35].

For all nozzle-plate spacings and equivalence ratios studied, the most prominent flame stabilization transition occurred when the flame changed from a nozzle-stabilized to a lifted flame as the nozzle Reynolds number increased above 2600. Below $Re = 2600$ nozzle-stabilized flames prevailed, while lifted flames were observed for $Re > 2600$. Nozzle-stabilized flames with equivalence ratios below $\Phi = 3$ were observed to lift off at Reynolds numbers less than 2600. The lifted flames mapped in Fig. 3 are further differentiated by the location of the flame stabilization point (see Fig. 2a). In general, increasing the Reynolds number for lifted flames pushes the location of the flame stabilization point away from the nozzle exit in the free jet, stagnation zone, or wall jet. Furthermore, varying the equivalence ratio changes the location where the methane and air are locally at stoichiometric proportions, and determines whether the combustion at the flame stabilization point is premixed or diffusion-controlled.

For most of the ranges of nozzle-plate spacing and equivalence ratio studied, the flame transitioned gradually from a nozzle-stabilized to a lifted, free jet-stabilized flame. Only for small nozzle-plate spacing, when the nozzle was in close proximity to the impingement plate, was the flame stabilization location a function of H. Otherwise, the flame stabilization was generally a function only of Re and Φ. The transition from free jet-stabilized flames to stagnation zone-stabilized flames results from increasing the Reynolds number or decreasing the equivalence ratio (see Fig. 3). There, the change in flow direction slows the local flow velocity, allowing the flame to stabilize. The flame shift downstream with decreasing equivalence ratio may suggest that the flame stabilization is more velocity-dependent as the flame transitions to premixed behavior. Decreasing the nozzle-plate spacing also forces the flame to stabilize in the stagnation zone, where the local velocity decreases enough to allow the flame to stabilize. As increases in Reynolds number or decreases in nozzle-plate spacing push the flame stabilization point past the stagnation zone into the wall jet, the flame abruptly stabilizes in the slower moving gases of the wall jet.

In the following sections, the aforementioned flame structures are discussed in detail and illustrated photographically. Nozzle-stabilized flames will be discussed first by describing a base case flame condition, followed by explorations of how the flame behavior is affected by changes in nozzle-plate spacing and equivalence ratio. Lifted flame behavior will then be discussed, also by describing a base case flame, followed by explanations of changes in flame structure as nozzle-plate spacing, equivalence ratio, and Reynolds number are varied. The observed flame structure will then be subsequently correlated to local, time-mean heat flux behavior.

5.2. Nozzle-stabilized flame

Fig. 4 shows nozzle-stabilized diffusion flame structures at $Re = 1500$ for varying Φ and H. These images are representative of all flame behavior observed for $Re < 2600$. Photographs proceeding from left to right in the figure indicate changes in flame structure due to increasing Φ, while changes due to increasing H are indicated by the photograph sequences from bottom to top. The experimental condition $\Phi = 4.0$ and $H = 15$ (Fig. 4a) is taken here as the base-case experimental condition. (It should be noted that the reflection of the flame in the polished aluminum impingement plate is visible for many of the flame photographs.) A thin layer of cool, unreacted gases separates the flame surface from the plate. Visual observations of the flame reveals that the flame surface in Fig. 4a was generally smooth and steady as H is increased up to a nozzle-plate spacing of 10 diameters, beyond which the flame began to flicker along the rest of the length of the free jet and the wall jet flame. At this low Reynolds number, buoyancy-induced vortices are observed to form between the ambient air and the region of hot gases surrounding the flame in the free jet. The vortices travel upward toward the plate with the hot buoyant gases, following the free jet, causing the flame to alternately bulge and shrink. These vortices have been documented and studied previously in several investigations of free jet flames [36–41]. It has been confirmed that a buoyancy-driven shear layer between the hot gases and the ambient air produces the outer vortical structures with characteristic frequencies between 5 and 20 Hz.

The flame in Fig. 4a impinges against the plate, negotiates the change in direction, then proceeds radially outward in the wall jet region where a visible flame separation from the wall is observed to increase with radial distance from the stagnation point. At a position $R \approx 3$, the flame is closest to the plate. It is speculated that as the combustion heats and expands the gases between the flame and the plate, the visible flame surface is pushed away from the plate as it flows radially outward

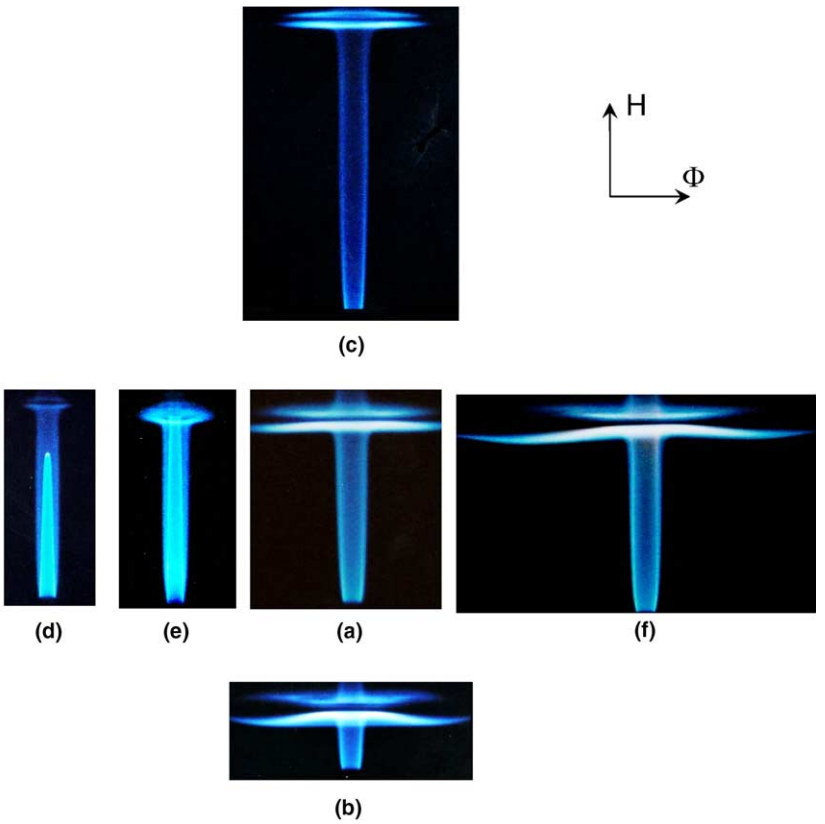

Fig. 4. Photographs of nozzle-stabilized flames with $Re = 1500$ at (a) $\Phi = 4.0$, $H = 15$; (b) $\Phi = 4.0$, $H = 5$; (c) $\Phi = 4.0$, $H = 25$; (d) $\Phi = 1.0$, $H = 15$; (e) $\Phi = 1.5$, $H = 15$; and (f) $\Phi = 7.0$, $H = 15$.

in the wall jet. This diffusion flame structure in Fig. 4a just described was observed with minor variation for all equivalence ratios greater than 2. Descriptions of the changes in the flame structure with height, equivalence ratio, and Reynolds number will follow.

The flame illustrated in Fig. 4b, at $Re = 1500$, $\Phi = 4$, and $H = 5$, shows changes in the observed flame structure that occur with a decrease in nozzle-plate spacing (relative to the base case). The diameter of the free jet at the stagnation zone is relatively smaller, and the minimum flame-plate spacing occurs at a smaller radial location. The most apparent difference between these two flames is the curvature of the wall jet flame from the impingement plate due to the rapidly expanding gases and the change in diameter of the wall jet flame. With a decrease in nozzle-plate spacing, there is less diffusion from the flame to the unreacted jet center. Consequently, the unburned gases are cooler and more fuel-rich when they reach the plate, and expand more in the process of heating and combustion. With the increase in the size of the wall jet flame, due the availability of fuel in the wall jet, Fig. 4b reveals that the flame curves back toward the plate at radial distances beyond approximately six diameters from the stagnation point. The flame curvature suggests that (i) buoyancy lifts the flame surface closer to the plate as the gases flow radially, and/or (ii) the location in the wall jet where the fuel–oxidizer proportions are stoichiometric is closer to the plate. Nozzle-stabilized flames at the same nozzle-plate spacing ($H = 5$) as the flame in Fig. 4b did not exhibit any visible oscillations in the free jet or the wall jet. Visible oscillations in both the free jet and the wall jet were detected only at nozzle-plate spacings greater than 10 diameters. At nozzle-plate spacings less than 10 diameters, the buoyancy-induced shear at the interface of the hot gases surrounding the flame and the ambient air are not sufficient for the development of vortices.

Fig. 4c shows a nozzle-stabilized flame at an increased nozzle-plate spacing, with $Re = 1500$, $\Phi = 4$, and $H = 25$. The most visible differences between Fig. 4a and c are the decrease radial extent of the visible wall jet flame and the decrease in the separation of the flame surface from the plate. The smaller wall jet flame is a result of more fuel being consumed in the free jet. The decrease in the separation of the flame surface from the plate may be a result of less expansion of the unburned gases at the plate as more combustion occurs in the pre-impingement jet than in the wall jet. As the nozzle-plate

distance is increased, more heat release occurs in the free jet and there is more time for the diffusion of hot products from the flame to the heart of the pre-impingement jet, such that the temperature of the unburned mixture increases. For this higher H, there was also an observed increase in the magnitude of the oscillations in the free jet flame with axial distance from the nozzle due to the buoyancy-driven vortices at the flame edge. These vortices were observed to grow in intensity with axial distance from the nozzle, causing the visible oscillations in the flame to be larger than those at smaller nozzle-plate spacings.

Fig. 4d and e show premixed flames at the same height and Reynolds number as the base case flame shown in Fig. 4a, but with reduced equivalence ratios of 1.0 and 1.5, respectively. The wall jet flame extends only a few diameters from the stagnation point for lower Φ: $R = 2$ for $\Phi = 1.0$ and $R = 3.5$ for $\Phi = 1.5$. Premixed flame characteristics for these nozzle-stabilized flames are observed at the same Reynolds numbers and equivalence ratio (for $\Phi < 2$) regardless of nozzle-plate spacing. An inner, premixed flame cone and an outer diffusion flame characterize the structure of these rich premixed flames. The transition from premixed to diffusion flame structure is apparent when comparing the flames of Fig. 4d and e: as the equivalence ratio is increased, the inner cone extends further upward and outward until it merges into the outer diffusion flame. For the premixed flames shown in Fig. 4d and e, there were no visible oscillations in the flow, suggesting the attenuation of the buoyancy-driven shear layer that can form vortices between the hot gases surrounding the flame and the ambient air. This is a result of the localized combustion in the premixed flame, in contrast to the spatially distributed combustion in the diffusion flame.

The effect of increased equivalence ratio is shown in Fig. 4f. Compared to Fig. 4a, there are no visible differences in the structure of the flame at the free jet and the stagnation zone. Comparing the curvature of the wall jet flame in Fig. 4a and f, it can be seen that the corresponding regions of both appear the same, except that the wall jet flame extends further radially and curves toward the plate for the flame with a higher equivalence ratio. The increase in the overall diameter of the wall jet flame is believed to be a result of the increase in the proportion of fuel in the unburned mixture. The increasing diameter of the wall jet flame with increased Φ was observed for equivalence ratios between 2 and 12.

5.3. Lifted flame

Generally speaking, lifted flames were observed for flames with $Re > 2600$ and $\Phi > 3$. Fig. 5 documents observed flame structures for lifted flames with a Reynolds number of 2800. The flame in Fig. 5a corresponding to $H = 15$ was observed to stabilize somewhat erratically approximately six diameters from the plate in the free jet. The radial extent of the wall jet flame is approximately 18 nozzle diameters. Despite the large equivalence ratio at the nozzle exit, the expected decrease in local equivalence ratio by the entrainment of ambient air, the brightness of the combustion at the flame stabilization point, and the localized deceleration of the flow field caused by the flow turn suggest premixed combustion occurs at the flame stabilization point in a distributed fashion. The apparent thickness of the combusting region at the flame stabilization point may also suggest the possibility of the formation of a multi-flame structure, as observed by Chen and Bilger [34] and Lyons and Watson [35]. In the wall jet, the flame transitions to a thin, irregular flame surface that exhibits more diffusion-controlled than premixed combustion characteristics. Although the flame does separate slightly from the plate along the wall jet, the separation is not as apparent as with the nozzle-stabilized flame. This suggests higher temperatures in the unburned mixture and products between the wall and the wall jet flame because of the distributed region of premixed combustion near the stagnation point upstream of the flame stabilization location. Fig. 5a also illustrates that the fluctuations in the flame structure in the wall jet are asymmetric. They were also observed to be unsteady.

The variation in the lifted flame structure with nozzle-plate spacing was influenced both by the free jet impingement on the plate and air entrainment. A flame with a Reynolds number of 2800 and an equivalence ratio of 5.2 was stabilized either in the stagnation zone ($5 \leqslant H \leqslant 8$) or the free jet ($H \geqslant 10$). For a flame with $Re = 5600$, there were two transitions that occurred with increasing height. For $H < 16.5$, the flame was observed to stabilize at the plate, downstream from the stagnation point. For $16.5 \leqslant H \leqslant 18$, the flame could not be stabilized at any point in the flow field without a pilot flame. For$H \geqslant 18$, the flame stabilized in the stagnation zone.

Fig. 5b shows the visible flame with the same equivalence ratio and Reynolds number as the flame shown in Fig. 5a ($Re = 2800$, $\Phi = 5.2$), but for a nozzle-plate spacing of five diameters. This condition results in a stagnation-zone-stabilized flame (see Fig. 3). This flame stabilizes at $R = 2$, and then spreads across the plate forming a single, thin, irregular flame surface extending radially along the plate out to $R \approx 23$. At the flame stabilization point, the flame appears to be diffusion-controlled. For an increase in nozzle-plate spacing to $H = 25$ (Fig. 5c) the flame may be classified as free-jet stabilized. Similar to the flame of Fig. 5a at $H = 15$, there is a region of premixed combustion where the flame stabilizes. With an increase in H, the flame stabilization point remains at the same general axial distance from the nozzle exit, but the length of the free jet flame increases. However, as evidenced by a brighter flame, the

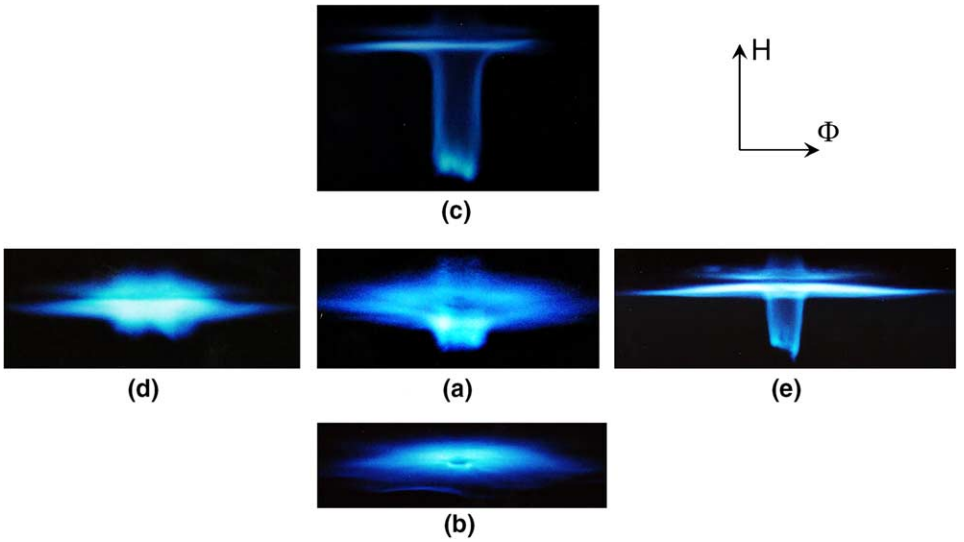

Fig. 5. Photographs of lifted flames with $Re = 2800$ at (a) $\Phi = 5.2$, $H = 15$; (b) $\Phi = 5.2$, $H = 5$; (c) $\Phi = 5.2$, $H = 25$; (d) $\Phi = 3.7$, $H = 15$; and (e) $\Phi = 8.9$, $H = 15$.

combustion appears to be more intense in the stagnation zone for $H = 15$ than 25.

The effect of decreasing the equivalence ratio (for the same Re and H) is illustrated in Fig. 5d, where $\Phi = 3.7$. In contrast to Fig. 5a ($\Phi = 5.2$), this flame is characterized by a localized region of apparent intense premixed combustion around the stagnation zone with a much smaller diffusion-controlled wall jet flame. The decrease in equivalence ratio, coupled with entrainment of ambient air in the free jet, appears to produce a large region of distributed premixed combustion as the jet impinges on the plate and transitions to a radial flow. This flame structure may be classified as stagnation-zone stabilized in the flame structure map of Fig. 3. Increasing the equivalence ratio to $\Phi = 8.9$ (Fig. 5e) relative to the base case condition reveals a transition to a more defined diffusion-controlled flame that stabilizes closer to the nozzle exit. A thin, irregular sheet of combusting gases extending from the free jet to the wall jet characterizes this flame. The flame stabilization point in the free jet tended to fluctuate vertically. Similar to flames discussed previously, the curvature of the wall jet flame produced by the heating and expansion of cool reactants is apparent in Fig. 5e. In the flame structure map shown in Fig. 3, the flame of Fig. 5e is classified as a free-jet stabilized flame.

In general, increasing the Reynolds number for lifted flames pushes the location of the flame stabilization point downstream from the nozzle exit in the free-jet, stagnation zone, or wall jet. Fig. 6 shows the flame structure with an increased Reynolds number $Re = 5600$ for $\Phi = 5.2$ and two nozzle-plate spacings, $H = 5$ and 15. The flame of Fig. 6a stabilizes at $R = 4$, and then extends radially outward to $R = 27$. As the nozzle-plate spacing is increased from 5 to 10, the flame stabilizes further from the stagnation point, and becomes brighter at the stabilization point, presumably due to the combined effect of increased entrainment and reduction in local flow velocity. Except for the bright ring where these flames stabilize, they appear much like other wall jet flames with a thin, irregular, diffusion-controlled flame surface. Fig. 6 also illustrates slight curvature in the flames away from, then back to the plate caused by expanding unburned gases. Wall jet-stabilized flames were observed over a wide range of equivalence ratios, generally occurring at higher Reynolds numbers (see Fig. 3).

6. Time-averaged heat transfer

The local time-mean heat flux is influenced significantly by all of the parameters varied in this study (Re, Φ, and H) because of their significant impact on flame structure as previously observed. The local heat flux depends on the proximity of the flame to the plate surface, the local or upstream combustion regime (predominantly diffusion or premixed conditions), and the local transport of heat, mass, and momentum. Generally speaking, these depend on the parameters Re, Φ, and H. Local, time-averaged heat flux measurements will be presented in the following sections. The data will focus first on nozzle-stabilized flame behavior, followed by lifted flame heat transfer characteristics. Finally, Reynolds number effects are detailed, spanning both the nozzle-stabilized and lifted flame regimes.

The local rate of heat release and molecular/turbulent transport of momentum, heat, and mass were not measured directly in this study. However, they have been inferred and compared from photographs of the flame structure discussed in the foregoing section. Thus, local heat flux is correlated qualitatively to the flame structure regime.

6.1. Nozzle-stabilized flame

Radial profiles of time-averaged measurements are shown in Fig. 7, illustrating (a) a typical profile for a nozzle-stabilized flame at $Re = 1500$, $H = 15$, and $\Phi = 4.0$, (b) the effect of nozzle-plate spacing for $Re = 1500$ and $\Phi = 4.0$, and (c) the effect of equivalence ratio for $Re = 1500$ and $H = 15$. Error bars (95% confidence) are also shown with the mean flux data. Corresponding flame structures have been discussed relative to the photographs of Fig. 4. Also shown in Fig. 7 is a variable termed the *Heating Value Fraction*, defined as the local fraction of the fuel (lower) heating value which has been dissipated convectively at the impingement plate between the stagnation point and a given radial location. The local heating value fraction is determined by integration of the local time-mean heat flux $q''(r)$ over the plate area for the radial location in question

$$\text{Heating Value Fraction} = \frac{\int_0^r q''(r')2\pi r'\,\mathrm{d}r'}{\dot{m}_{\text{fuel}}\text{LHV}} \tag{1}$$

where $\dot{m}_{\text{fuel}}$ and LHV are the fuel mass flow rate and lower heating value, respectively. This parameter represents, in a sense, a local measure of the combined combustion/heat transfer efficiency. Increases in combustion efficiency (conversion of fuel to products + heat) and/or convective heat transfer effectiveness result in an attendant increase in the local heating value fraction.

The radial mean heat flux profile shown in Fig. 7a is for a flame with $Re = 1500$, $\Phi = 4.0$, and $H = 15$ (see corresponding flame photograph in Fig. 4a). At these experimental conditions the mean heat flux is negative at the stagnation point, indicating that the impinging unburned gases in the pre-impingement jet core cools the hotter plate. Downstream (radially) of the stagnation point, the heat flux increases sharply and reaches a maximum value of about 25 kW/m^2 in the region where the wall-jet flame is closest to the plate ($R \approx 3$). As the flame begins to curve away from the plate ($R > 5$), the mean heat flux decreases, as the remaining methane is burned and the flame separation distance from the plate further decrease in the radial direction. The tip of the visible wall jet flame was at $R \approx 10$. Beyond $R = 11$, there is a sharp decrease in heat flux resulting from both the absence of combustion and the decrease in the temperature and velocity of the gases as they flow radially outward in the wall jet. The radial variation of the flame's heating value fraction dissipated convectively begins at zero at the stagnation point, then rises monotonically to a peak magnitude of 25% at $R = 15$.

Fig. 7b shows radial mean heat flux profiles at $Re = 1500$ and $\Phi = 4.0$ for flames at normalized nozzle-plate spacings of 5, 15, and 25 (see corresponding flame structure photographs in Fig. 4b, a, and c, respectively). The last radial positions for which measurements were made indicate where the visible flame ends. The stagnation heat fluxes in Fig. 7b reveal negative fluxes at the stagnation point for nozzle-plate spacings of 5 and 15 nozzle diameters, again corresponding to the cool potential core impinging on the plate. At $H = 25$, the cool core no longer exists because the radially inward diffusion of hot combustion products in the free jet reaches the jet centerline, resulting in higher gas temperatures. In general, Fig. 7b shows an increase in local mean heat flux with nozzle-plate spacing at all radial locations. This observation is also related to the gradual elimination of the potential core along the jet axial direction due to the diffusion of hot combustion products toward the jet centerline, causing the average temperature between the jet and the plate to increase, thus resulting in higher mean heat fluxes. For the same initial fuel quantity (same Re and Φ), smaller amounts of fuel remain to be burned after the flow impinges against the plate and turns for increasing H, resulting in wall-jet flames of decreasing diameter and corresponding decrease in the effective plate heating surface area as shown in Fig. 7b. The variation of heating value fraction dissipated convectively follows the same trend as the local mean heat flux for these conditions. For a given radial location, the flame with higher nozzle-plate spacing exhibits more effective transfer of the fuel's heating value to the impingement plate. As explained previously, this

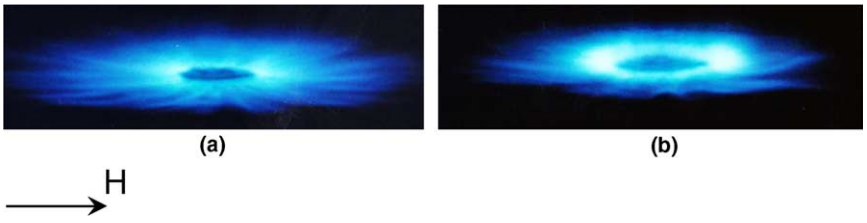

Fig. 6. Photographs of flames stabilized in the wall jet at $Re = 5600$, $\Phi = 5.2$ and (a) $H = 5$ or (b) $H = 10$.

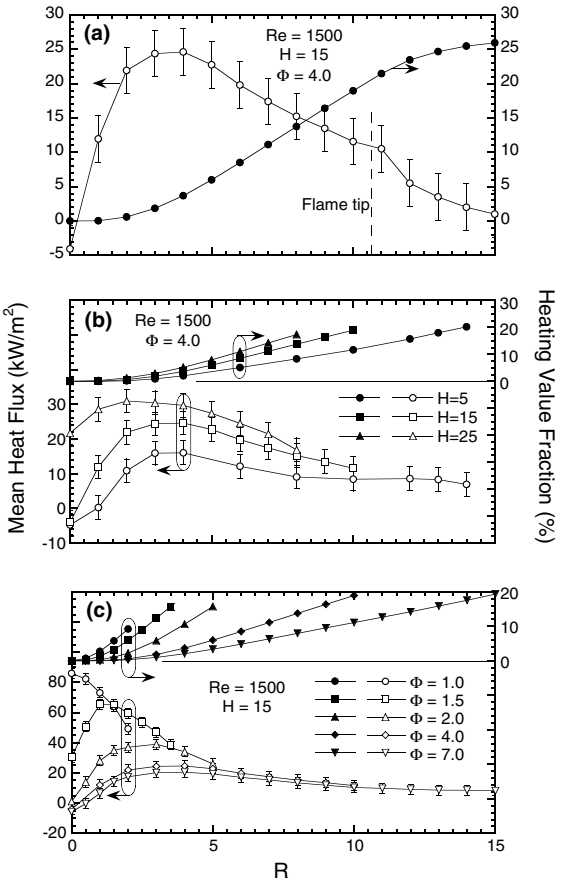

Fig. 7. Radial profiles of local mean heat flux and fraction of fuel heating value dissipated convectively for flames with $Re = 1500$, illustrating (a) a typical profile for a flame with $\Phi = 4.0$, and $H = 15$; (b) the effect of various nozzle-plate spacings at $\Phi = 4.0$; and (c) the effect of various equivalence ratios at $H = 15$.

is likely due to the increased diffusion of oxygen to the unreacted central flow in the pre-impingement jet. Interestingly, the heating value fraction never exceeds approximately 20% for a radius of 15 jet diameters, indicating that the majority of the impinging flame's chemical/thermal energy remains in the radial flow. It is further noted that even for cases where peak heat fluxes occur in the stagnation zone (e.g., $H = 25$), very little of the flame jet's available energy is transferred to the plate in the stagnation zone due to the small area.

The effect of a transition from premixed to diffusion-controlled burning on the radial mean heat flux is illustrated Fig. 7c, which shows radial profiles of heat flux and heating value fraction for flames with a Reynolds number of 1500, nozzle-plate spacing of 15 diameters, and equivalence ratios ranging from 1.0 to 7.0. Corresponding photographs of flame structure are shown in Fig. 4d, e, a, and f, respectively, for $\Phi = 1.0$, 1.5, 4.0, and 7.0. For $\Phi = 1.0$, the maximum heat flux occurs at the stagnation point. As Φ is increased, the peak heat flux moves radially away from the stagnation point as the unburned core of the premixed flame lengthens and impinges against the plate. Once the premixed flame transitions to a diffusion flame ($\Phi \geqslant 2.0$), the radial mean heat flux profiles are similar because the flame structure in the pre-impingement jet and around the stagnation zone changes little for the diffusion flame structure (compare Fig. 4a and f). The stagnation heat flux magnitude and the radial location of the maximum heat flux are nearly the same for $\Phi > 2.0$. Heat flux maxima for all of the diffusion flames are located at $R \approx 3$, where the flame was closest to the impingement plate. The only significant difference is the increase in the effective plate heating surface area associated with the increase in the wall-jet flame diameter as the equivalence ratio increases from 4.0 to 7.0, since it requires longer to burn a richer mixture for a given Reynolds number and nozzle-plate spacing.

The fraction of the impinging flame's heating value dissipated convectively at a given radial location increases for greater premixing of the flame jet (decreasing Φ). It is not surprising that premixed flames are more effective at transferring available flame energy to the plate, since the energy release is not limited by oxygen diffusion to the fuel. The radial gradient (rate) of heating value energy transfer is also observed to be significantly higher for lower values of the equivalence ratio Φ. It is again noted that the fraction of the flame's heating value transferred to the plate never exceeds 20%.

6.2. Lifted flame

Radial mean heat flux profiles for lifted flames are shown in Fig. 8, illustrating in the respective panels (a) the effect of nozzle-plate spacing for $Re = 2800$ and $\Phi = 5.2$, (b) the effect of equivalence ratio for $Re = 2800$ and $H = 15$, and (c) the effect of nozzle-plate spacing for $Re = 5600$ and $\Phi = 5.2$. Corresponding photographs of the flame structure have been shown and discussed in Figs. 5 and 6.

Fig. 8a illustrates heat flux and heating value fraction profiles for lifted flames at an equivalence ratio of 5.2, a Reynolds number of 2800, and nozzle-plate spacings of 5, 15, and 25 nozzle diameters. Photographs of these three flames are shown in Fig. 5b, a, and c, respectively. The trends are similar for all nozzle-plate spacings. The mean flux increases from the jet centerline to a maximum value at a radial location $R \approx 6$–8, then decreases radially toward the edge of the flame in the wall jet region. By comparison with the nozzle-stabilized flame data of Fig. 7, the maximum heat flux occurs further from the stagnation point for lifted flames. The profile for the flame at $H = 5$ in Fig. 8a reveals negative heat fluxes in the stagnation region, again resulting from

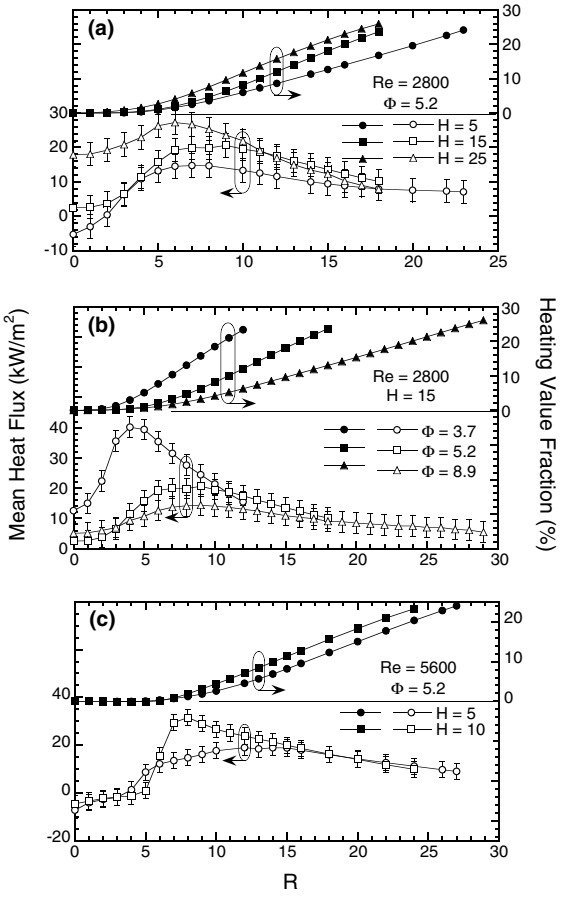

Fig. 8. Radial profiles of local mean heat flux and fraction of fuel heating value dissipated convectively for lifted flames: (a) the effect of various nozzle-plate spacings at $Re = 2800$, $\Phi = 5.2$; (b) the effect of various equivalence ratios at $Re = 2800$, $H = 15$; and (c) the effect of nozzle-plate spacing at $Re = 5600$, $\Phi = 5.2$.

impingement of the cool, unreacted jet. The region of highest heat flux, $4 \leqslant R \leqslant 8$, corresponds to the region of flame proximity to the impingement plate. Beyond a radial location of eight diameters, the flame is pushed away from the plate by expanding gases, and the resulting heat flux gradually decreases with radial distance. Correlating the observed flame structures for $H = 5$ and 15 in Fig. 5b and a, respectively, with the corresponding heat flux profiles in Fig. 8a suggests a slower heat release along the wall for smaller nozzle-plate spacings, resulting in lower heat fluxes and associated lower variation in mean flux with radial distance from the stagnation point.

Comparing the heat flux profiles for the flames at nozzle-plate spacings of $H = 15$ and 25 in Fig. 8a shows that the increase in nozzle-plate spacing yields higher heat fluxes at all radial locations along the impingement plate up to a location of 12 diameters from the stagnation point. The higher mean flux for the flame with a nozzle-plate spacing of 25 diameters is a result of the greater diffusion (molecular or turbulent transport) that occurs in the free jet prior to its impingement against the plate. Recall from the discussion of observed flame structure for these cases that the difference in the combustion at the flame stabilization point suggested greater interaction between the impinging jet and the plate for $H = 15$, slowing the local flow velocity and increasing the combustion intensity at the plate. Fig. 8a also reveals higher heating value fraction at a given radial location for increased nozzle-plate spacing.

Fig. 8b illustrates the radial heat flux and combustion/heat transfer efficiency behavior for flame jets with nozzle-plate spacing of 15 diameters, Reynolds number of 2800, and varying equivalence ratios of 3.7, 5.2, and 8.9 (see the flame photographs in Fig. 5d, a, and e, respectively). The mean heat flux profile for the stagnation zone-stabilized flame ($\Phi = 3.7$) reveals a rapid heat flux increase with radial distance from the stagnation point, a peak at $R = 4$, followed by a gradual decrease. The peak corresponds to the brightest region of the flame, where the maximum heat release occurs. Beyond $R = 4$, the flame is controlled by diffusion as the remaining fuel is reacted, and the heat flux decreases rapidly with distance from the stagnation point. The heat flux profile for $\Phi = 8.9$ (see the photograph of Fig. 5e) reveals an increased stagnation heat flux compared to the $\Phi = 5.2$ condition. However, the heat flux along the wall jet is lower for most of the radial distance along the plate than for flames at $\Phi = 3.7$ and $\Phi = 5.2$. Comparing the corresponding flame structures shown in Fig. 5d with Fig. 5a, the flame stabilization point and the wall jet flame suggest more diffusion-controlled combustion than what was observed for lower equivalence ratios. This would have the effect of delaying the heat release, resulting in lower heat fluxes as observed. As with the nozzle-stabilized flame jets, increasing the level of premixing in the flame increases the heating value fraction. Fig. 8b shows, as expected, that the fraction of fuel heating value that is transported to the wall is considerably higher for greater premixing (lower Φ). The effect of equivalence ratio on the heating value fraction is much stronger than either Reynolds number or nozzle-plate spacing.

The radial heat flux profiles in Fig. 8c are for Reynolds number of 5600 (lifted flame), equivalence ratio of 5.2, and nozzle-plate spacings of 5 and 10 diameters (see the flame photographs in Fig. 6a and b). Recall from the previous discussion on flame structure that at these conditions, the flame is stabilized in the wall jet region 3–6 diameters downstream from the stagnation point. In Fig. 8c, the flame at $H = 5$ exhibits negative wall heat flux radially out to the flame stabilization point at $R = 4$, after which the heat flux increases rapidly with radius. The points of maximum heat flux do not

correspond to the region where the flame is closest to the plate. Rather, there is a wide radial band of increasing heat flux up to $R = 12$, and then beyond $R = 15$ the heat flux gradually decreases. The heat flux in the wall jet of this flame is higher than other wall jet heat fluxes, as shown in Fig. 8a and b. This is a result of both the heat release occurring entirely in the wall jet, as well as having twice the mass flow rate of fuel and air in the jet mixture. The heat flux profile for the flame with $H = 10$ shows similar behavior along the surface of the plate, with the exception of a more rapid increase in mean flux in the radial region $5 \leqslant R \leqslant 7$. Negative wall heat fluxes prevail radially out to the flame stabilization point, and then a sharp increase occurs at $R = 5$. The much higher heat fluxes for the flame at $H = 10$, in comparison to that at $H = 5$, may be attributed to the premixed combustion at the flame stabilization point, which results from the greater quantity of air entrained in the free jet, lowering the local equivalence ratio. As observed in Fig. 8a, increasing the nozzle-plate spacing increases the fraction of flame energy dissipated convectively at a given radial location.

6.3. Reynolds number dependence

Nozzle-stabilized flame (low-*Re*) and lifted flame (high-*Re*) behavior has been presented in the foregoing sections. As a bridge between these two different flame structure scenarios, Fig. 9 is presented, illustrating the effect of nozzle-plate spacing and equivalence ratio on the mean stagnation heat flux for nozzle Reynolds numbers spanning both the nozzle-stabilized and lifted flame regimes (see Fig. 3).

Fig. 9a shows the change in mean stagnation heat flux with nozzle-plate spacing for diffusion flames (high Φ) with Reynolds numbers of 1500 (nozzle-stabilized flame), and 2800 and 5600 (lifted flames). Examination of the heat flux for the nozzle-stabilized flame ($Re = 1500$) reveals that up to a nozzle-plate spacing of $H \approx 20$, the heat flux is negative and nearly independent of H. At nozzle-plate spacings greater than 20 diameters, the stagnation heat flux increases slowly with height. As explained previously, this gradual increase in stagnation heat flux is caused by the elimination of the unreacted core by radially inward thermal and mass diffusion in the pre-impingement flame. Further increases in nozzle-plate spacing provides greater distance for diffusion to raise the temperature of the core, increasing the temperature gradient between the hot gases and the cooled plate and thus increasing the mean stagnation heat flux.

For the lifted flame conditions of Fig. 9a ($Re = 2800$ and 5600), the stagnation zone-stabilized flame yields a gradual decrease in heat flux as the increasing dominance of diffusion for equivalence ratio in the range $3 \leqslant \Phi \leqslant 5$ slowed the rate of heat release. Recall from the discussion of flame structure that the behavior of

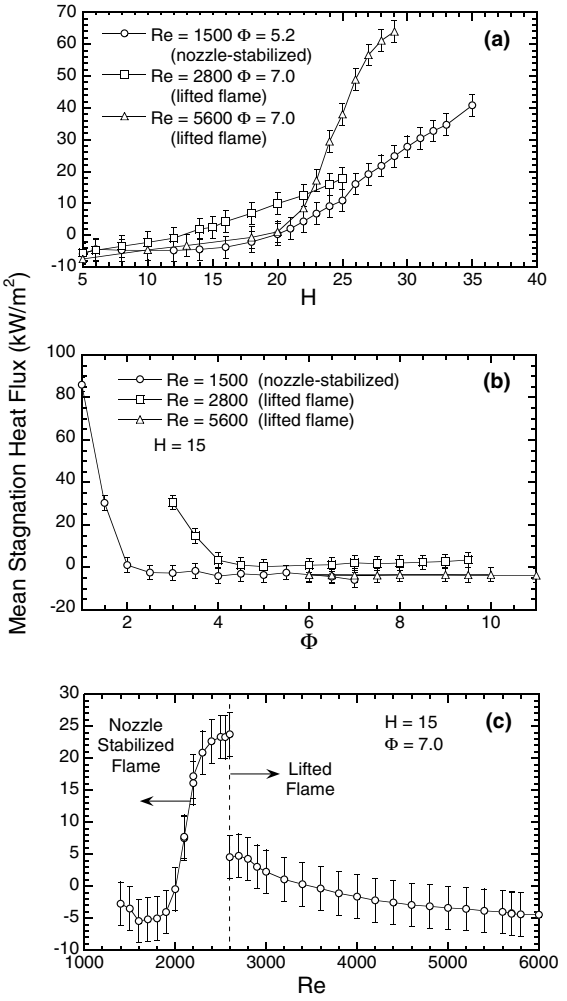

Fig. 9. Mean stagnation heat flux measurements as a function of (a) nozzle-plate spacing, (b) equivalence ratio for $H = 15$, and (c) Reynolds number for $\Phi = 7.0$.

these flames suggests premixed combustion due to the rapid heat release at the flame stabilization point and the entrainment of air between the nozzle and plate. At $\Phi \geqslant 6$, the flame transitions to free jet-stabilized combustion, and there is a gradual increase in heat flux as the flame stabilizes further upstream in the pre-impingement jet, increasing the thermal transport to the unburned gases in the jet. For the wall jet-stabilized flame ($6 \leqslant \Phi \leqslant 6.5$) and the stagnation zone-stabilized flame ($7 \leqslant \Phi \leqslant 12$) at $Re = 5600$, cool unburned gases impinge against the plate, producing a negative heat flux that changes only moderately with the equivalence ratio.

Fig. 9b illustrates the change in mean stagnation heat flux as a function of equivalence ratio for flames with Reynolds numbers of 1500 (nozzle-stabilized flame), and 2800 and 5600 (lifted flame) for a nozzle-plate spac-

ing of $H = 15$. The three Reynolds numbers illustrate the full range of flame stabilization location behavior. For an equivalence ratio of $\Phi = 1.0$ at $Re = 1500$, the premixed flame reaction is nearly complete prior to its impingement on the plate (as illustrated in the flame photograph of Fig. 4d), resulting in the maximum heat flux at the stagnation point (see Fig. 9b). The stagnation flux behavior for $1.0 \leqslant \Phi \leqslant 3.0$ is illustrative of the transition from a premixed conical flame reacting in the heart of the free jet and burning completely prior to impingement, to a diffusion flame combusting at the interface between the core and the ambient air and persisting radially beyond the stagnation point. As the inner cone of the premixed flame stretches upward and outward with increasing equivalence ratio, the stagnation heat flux decreases dramatically from approximately 85 kW/m^2 at $\Phi = 1.0$ to 1.1 kW/m^2 at $\Phi = 3.0$. At higher equivalence ratios, all of the stagnation heat fluxes are observed to be negative and nearly independent of equivalence ratio.

Fig. 9c shows the variation of stagnation heat flux with increasing nozzle Reynolds number for an equivalence ratio of 7.0 and a nozzle-plate spacing of 15 nozzle diameters. In the nozzle-stabilized diffusion flame regime ($\Phi > 3.0$) the behavior is similar regardless of the equivalence ratio. Premixed flames ($1.0 \leqslant \Phi \leqslant 2.0$) were not observed for $Re > 2400$. The stagnation heat flux variation with Reynolds number for nozzle-stabilized flames is related to the axial length of the potential core. While the potential core extends up to or past the plate location, an unreacted, low-temperature mixture at inlet conditions reaches the stagnation area, cooling the plate and resulting in negative stagnation heat fluxes. This trend is evident up to a Reynolds number near 1800, where the stagnation heat flux begins to increase with Reynolds number (see Fig. 9c). As the Reynolds number is increased, the length of the potential core is reduced by the increased radial transport of hot combustion products from the flame to the jet core, increasing the temperature of the unburned mixture along the jet centerline. The net result is an increase in the heat flux to the plate at the stagnation point with increasing Re. This trend of increasing stagnation heat flux continues up to a Reynolds number of 2600, after which the flame experiences a transition from a nozzle-stabilized to a lifted flame. The transition from nozzle-stabilized to lifted flame behavior was found to occur over a range in Reynolds number ($Re = 2600 \pm 100$ at the conditions shown). Thus, although shown as occurring simultaneously in Fig. 9c, the mean stagnation flux at the transition Reynolds number is either that characteristic of the nozzle-stabilized or lifted flame in this region, but not both. With further increases in Reynolds number, the flame stabilization point is pushed further downstream in the wall jet. This decreases the transport of hot combustion products with the free jet relative to that which occurs for nozzle-stabilized flames for $2100 \leqslant Re \leqslant 2600$. Consequently, there is a general decrease in heat flux as the Reynolds number increased and the flame stabilization point transitions from the free jet-stabilized to the stagnation zone-stabilized regimes ($Re \approx 4000$), and then to wall jet-stabilized behavior ($Re \approx 5700$).

7. Conclusions

Flame behavior and time-averaged local heat flux were observed and measured, respectively, for impinging methane–air jet flames with nozzle Reynolds numbers in the range between 1500 and 6000, equivalence ratios between 1 and 9, and non-dimensional nozzle-plate spacings between 5 and 35 nozzle diameters. At Reynolds numbers of 1500, flame photographs and observation reveal symmetric, laminar flame surfaces. At nozzle-plate spacings greater than ten diameters, vortices in the free jet and the wall jet begin to produce oscillations in the flame surface. The laminar flames with equivalence ratios less than two exhibit classic premixed flame behavior. At higher equivalence ratios, a diffusion flame structure was observed. With increasing equivalence ratio, the wall jet flame increases in size while the flame at the free jet and stagnation zone remains unchanged. Lifted flames result for Reynolds numbers greater than 2600. Lifted flames were observed to stabilize in the free jet, at the stagnation zone, and in the wall jet. The flame stabilization point was pushed downstream by increases in Reynolds number, and were observed to remain in the same downstream location, with respect to the nozzle, as the nozzle-plate spacing was increased. Varying the equivalence ratio was seen to change the location where the methane and air were at stoichiometric proportions and whether the combustion at the flame stabilization point was premixed or diffusion-controlled.

Generally speaking, premixed flames are observed to yield the highest heat fluxes measured in this study, exhibiting substantially higher heat fluxes than diffusion flames due to the more rapid and localized heat release. Conversely, diffusion-stabilized flame structures yield slower heat release and larger overall flame structures, resulting in lower heat fluxes over larger areas. Heat fluxes are also seen to increase as the rate of molecular or turbulent transport increase at, or upstream, of any radial location on the impingement plate. Increased transport rates also affect the local heat flux by the increased rates of heat release caused by a decrease in local equivalence ratios due to air entrainment. Increased transport rates result from increases in Reynolds number and/or the axial length of the pre-impingement jet, which allow greater distance for transport to occur and the development of transitional and turbulent mixing structures.

References

[1] R. Viskanta, Convective and radiative flame jet impingement heat transfer, Int. J. Transport Phenom. 1 (1998) 1–15.

[2] C.E. Baukal, B. Gebhart, A review of flame impingement heat transfer studies. Part 2: Measurements, Combust. Sci. Technol. 104 (1995) 359–385.

[3] R. Viskanta, Enhancement of heat transfer in industrial combustion systems: Problems and future challenges, in: J.R. Lloyd, Y. Kurosaki (Eds.), Proceedings of the 3rd ASME/JSME Thermal Engineering Joint Conference—1991, vol. 5, ASME, New York, 1991, pp. 161–173.

[4] R. Viskanta, Heat transfer to impinging isothermal gas and flame jets, Exp. Thermal Fluid Sci. 6 (1993) 111–134.

[5] G.K. Hargrave, M. Fairweather, J.K. Kilham, Forced convective heat transfer from premixed flames. Part 1: Flame structure, Int. J. Heat Fluid Flow 8 (1987) 55–63.

[6] G.K. Hargrave, M. Fairweather, J.K. Kilham, J.K. Forced, convective heat transfer from premixed flames. Part 2: Impingement heat transfer, Int. J. Heat Fluid Flow 8 (1987) 132–138.

[7] C.E. Baukal, B. Gebhart, A review of flame impingement heat transfer studies. Part 1: Experimental conditions, Combust. Sci. Technol. 104 (1995) 339–357.

[8] C.E. Baukal, B. Gebhart, A review of empirical flame impingement heat transfer correlations, Int. J. Heat Fluid Flow 17 (1996) 386–396.

[9] C.E. Baukal, B. Gebhart, A review of semi-analytical solutions for flame impingement heat transfer, Int. J. Heat Mass Transfer 39 (1996) 2989–3002.

[10] Y. Zhang, K.N.C. Bray, Characterization of impinging jet flames, Combust. Flame 116 (1999) 671–674.

[11] T. Foat, K.P. Yap, Y. Zhang, The visualization and mapping of turbulent premixed impinging flames, Combust. Flame 125 (2001) 839–851.

[12] H.H. Liakos, E.P. Karamida, M.A. Founti, N.C. Markatos, Heat and mass transfer study of impinging turbulent premixed flames, Heat Mass Transfer 38 (2002) 425–432.

[13] R.P. Lindstedt, E.M. Vaos, Second moment modeling of premixed turbulent flames stabilized in impinging jet geometries, Proceedings Symposium (International) on Combustion, vol. 1, 1998, pp. 957–962.

[14] L.L. Dong, C.W. Leung, C.S. Cheung, Combustion optimization of a slot flame jet impingement system, J. Inst. Energy 76 (2003) 80–88.

[15] L.L. Dong, C.W. Leung, C.S. Cheung, Heat transfer characteristics of an impinging butane/air flame jet of low Reynolds number, Exp. Heat Transfer 14 (2001) 265–282.

[16] L.L. Dong, C.W. Leung, C.S. Cheung, Heat transfer characteristics of premixed butane/air jet impinging on an inclined flat surface, Heat Mass Transfer 39 (2002) 19–26.

[17] L.L. Dong, C.W. Leung, C.S. Cheung, Heat transfer from an impinging premixed butane/air slot flame jet, Int. J. Heat Mass Transfer 45 (2002) 979–992.

[18] L.C. Kwok, C.W. Leung, C.S. Cheung, Heat transfer characteristics of slot and round premixed impinging flame jets, Exp. Heat Transfer 16 (2003) 111–137.

[19] J.R. Rigby, B.W. Webb, An experimental investigation of diffusion flame jet impingement heat transfer, in: L.S. Fletcher, T. Aihara (Eds.), Proceedings of the ASME/JSME Thermal Engineering Joint Conference 1995, vol. 3, ASME, New York, 1995, pp. 117–126.

[20] J. Wu, J. Seyed-Yagoobi, R.H. Page, Heat transfer and combustion characteristics of an array of radial jet reattachment flames, Combust. Flame 125 (2001) 955–964.

[21] G.K. Malikov, D.L. Lobanov, K.Y. Malikov, V.G. Lisienko, R. Viskanta, A.G. Fedorov, Direct flame impingement heating for rapid thermal materials processing, Int. J. Heat Mass Transfer 44 (2001) 1751–1758.

[22] G.K. Malikov, D.L. Lobanov, K.Y. Malikov, V.G. Lisienko, R. Viskanta, A.G. Fedorov, Experimental and numerical study of heat transfer in a flame jet impingement system, J. Inst. Energy 72 (1999) 2–9.

[23] L.L. Dong, C.W. Leung, C.S. Cheung, Heat transfer from a row of three butane/air flame jets impinging on a flat plate, Int. J. Heat Mass Transfer 46 (2003) 113–125.

[24] L.L. Dong, C.W. Leung, C.S. Cheung, Heat transfer and wall pressure characteristics of twin premixed butane/air flame jets, Int. J. Heat Mass Transfer 47 (2004) 489–500.

[25] L.L. Dong, C.W. Leung, C.S. Cheung, Heat transfer characteristics of a pair of impinging rectangular flame jets, J. Heat Transfer 125 (2003) 1140–1146.

[26] A. Barnes, Heat flux sensors. Part 1: Theory, Vatell Corporation, Blacksburg, Virginia, 1999. Available from: <http://www.vatell.com/heatflux/index.html>.

[27] R.J. Moffat, Describing the uncertainties in experimental results, Exp. Thermal Fluid Sci. 1 (1988) 3–17.

[28] S.G. Tuttle, Characterization of local, time-mean and time-resolved heat transfer from an impinging flame jet, M.S. Thesis, Brigham Young University, 2002, Provo, UT.

[29] S.R. Turns, An Introduction to Combustion, second ed., McGraw-Hill, Boston, MA, 2000.

[30] I. Glassman, Combustion, third ed., Academic Press, San Diego, CA, 1996.

[31] C.J. Poscillico, S. Lederman, Laser diagnostics of reacting stagnation point flows, AIAA J. 27 (1989) 67–78.

[32] W.R. Hawthorne, D.B. Weddel, H.C. Hottel, Mixing and combustion in turbulent gas jets, in: Third Symposium on Combustion Flame and Explosion Phenomena, Williams & Wilkins, Baltimore, MD, 1949, pp. 266–285.

[33] R.W. Schefer, M. Namazian, J. Kelly, Stabilization of lifted turbulent jet flames, Combust. Flame 99 (1994) 75–86.

[34] Y.-C. Chen, R.W. Bilger, Stabilization mechanisms in axisymmetric jet flows, Combust. Flame 123 (2000) 23–45.

[35] K.M. Lyons, K.A. Watson, Partially premixed combustion in lifted turbulent jets, Combust. Sci. Technol. 156 (2000) 97–105.

[36] I. Kimura, Stability of laminar jet-flames, 10th Symposium (Int'l) on Combustion, The Combustion Institute, Pittsburgh, Pennsylvania, 1965, pp. 1295–1301.

[37] R. Matsumoto, T. Nakajima, K. Kimoto, S. Noda, S. Maeda, An experimental study on low frequency oscillations and flame generated turbulence in premixed diffusion flames, Combust. Sci. Technol. 27 (1982) 103–111.

[38] A.J. Yule, N.A. Chigier, S. Ralph, R. Boulderstone, J. Ventura, Combustion–transition interaction in a jet flame, AIAA J. 19 (1981) 752–760.

[39] W.M. Roquemore, L.-D. Chen, L.P. Goss, W.F. Lynn, The structure of jet diffusion flames, in: R. Borghi, S.N.B.

Murthy (Eds.), Lecture Notes in Engineering, vol. 40, Springer-Verlag, Berlin, pp. 49–88.

[40] V.R. Katta, W.M. Roquemore, Role of inner and outer structures in transitional jet diffusion flames, Combust. Flame 92 (1993) 274–282.

[41] M.Q. McQuay, S.M. Cannon, Time-resolved temperature measurements in the developing region of an elliptic, jet diffusion flame at a Reynolds number of 6000, Combust. Sci. Technol. 119 (1996) 13–33.